

Chemical Trends of the Bulk and Surface Termination-Dependent Electronic Structure of Metal-Intercalated Transition Metal Dichalcogenides

Brendan Edwards, Darius-A. Deaconu, Philip A. E. Murgatroyd, Sebastian Buchberger, Tommaso Antonelli, Daniel Halliday, Gesa-R. Siemann, Andela Zivanovic, Liam Trzaska, Akhil Rajan, Edgar Abarca Morales, Daniel A. Mayoh, Amelia E. Hall, Rodion V. Belosludov, Matthew D. Watson, Timur K. Kim, Deepnarayan Biswas, Tien-Lin Lee, Craig M. Polley, Dina Carbone, Mats Leandersson, Geetha Balakrishnan, Mohammad Saeed Bahramy,* and Phil D. C. King*

Cite This: <https://doi.org/10.1021/acs.chemmater.4c00824>

Read Online

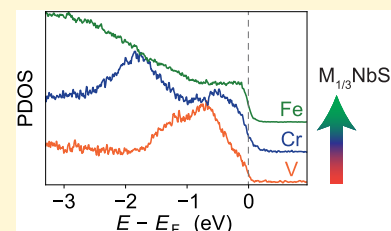
ACCESS |

Metrics & More

Article Recommendations

Supporting Information

ABSTRACT: The addition of metal intercalants into the van der Waals gaps of transition metal dichalcogenides has shown great promise as a method for controlling their functional properties. For example, chiral helimagnetic states, current-induced magnetization switching, and a giant valley-Zeeman effect have all been demonstrated, generating significant renewed interest in this materials family. Here, we present a combined photoemission and density-functional theory study of three such compounds: $V_{1/3}\text{NbS}_2$, $\text{Cr}_{1/3}\text{NbS}_2$, and $\text{Fe}_{1/3}\text{NbS}_2$, to investigate chemical trends of the intercalant species on their bulk and surface electronic structure. Our resonant photoemission measurements indicate increased hybridization with the itinerant NbS_2 -derived conduction states with increasing atomic number of the intercalant, leading to pronounced mixing of the nominally localized intercalant states at the Fermi level. Using spatially and angle-resolved photoemission spectroscopy, we show how this impacts surface-termination-dependent charge transfers and leads to the formation of new dispersive states of mixed intercalant-Nb character at the Fermi level for the intercalant-terminated surfaces. This provides an explanation for the origin of anomalous states previously reported in this family of compounds and paves the way for tuning the nature of the magnetic interactions in these systems *via* control of the hybridization of the magnetic ions with the itinerant states.



1. INTRODUCTION

Transition metal dichalcogenides (TMDs) have become the subject of intensive research, owing to the diverse properties they host.^{1–3} These include metallic and insulating electronic structures,⁴ several notable examples of spin-valley locking,^{5–9} collective phenomena such as charge density waves and superconducting states,^{10–14} and a myriad of topological phases.^{15–17} Intercalating magnetic transition metal ions into the van der Waals gap of 2H-TMDs has emerged as a powerful method to further stabilize novel magnetic states and textures, where the intercalant species nominally act as local magnetic moments.^{18,19} At critical concentrations, they occupy periodic sites that break the centrosymmetry of the host compounds. This allows for the presence of antisymmetric Dzyaloshinskii–Moriya exchange interactions, which underpin the formation of a host of noncollinear magnetic orders.^{20–22}

Here, we investigate intercalated TMDs of the form $M_{1/3}\text{NbS}_2$, where $M = (\text{V}, \text{Cr}, \text{and Fe})$. At this critical composition, the intercalants occupy interstitial sites to form a superlattice, which generates a new periodic potential with a $\sqrt{3} \times \sqrt{3}R30^\circ$ periodicity.²³ The resulting crystal structure is

shown in Figure 1a, where it can be seen that the intercalants form distorted octahedral coordination environments with the surrounding S ligands.²⁴ The distance between adjacent intercalants is too large for significant direct exchange interactions. Instead, the magnetism must be mediated through the NbS_2 layers, and thus the dominant exchange interaction in these compounds is frequently thought to be a Ruderman–Kittel–Kasuya–Yosida (RKKY) mechanism.¹⁸ In this scenario, the modulation of the NbS_2 electronic structure that results from the intercalation is described by a rigid band shift picture, where there is an ionic charge transfer of electrons from intercalant 3d and 4s orbitals into the Nb 4d orbitals with minimal hybridization between the intercalant- and Nb-derived states, leaving the electronic structure otherwise unperturbed.

Received: March 20, 2024

Revised: July 9, 2024

Accepted: July 10, 2024

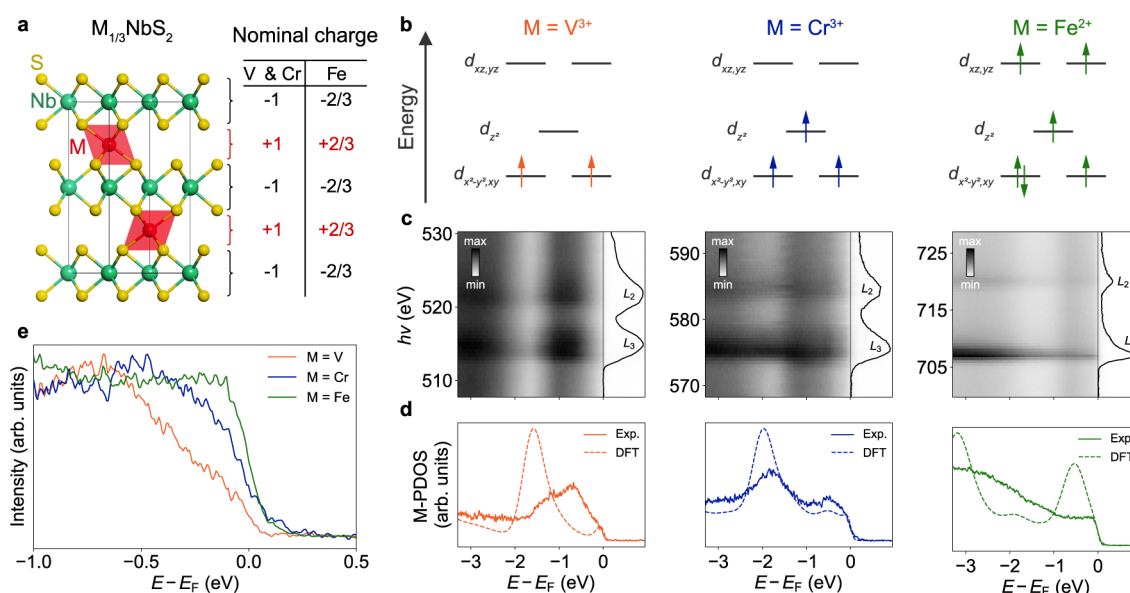


Figure 1. Electronic structure of $M_{1/3}\text{NbS}_2$ compounds. (a) Crystal structure displaying the intercalant-dependent electronic charge of layers described by a simple ionic picture. The intercalants are surrounded by S ligands in octahedral-like coordination environments, as indicated by shaded red regions. (b) Schematics illustrating the crystal field splitting and electron filling of the 3d intercalant orbitals in $V_{1/3}\text{NbS}_2$, $\text{Cr}_{1/3}\text{NbS}_2$, and $\text{Fe}_{1/3}\text{NbS}_2$, after ref 24. While V and Cr atoms possess +3 oxidation states, Fe atoms will exist in +2 oxidation states. (c) Angle-integrated ResPES spectra ($T = 27$ K, LH polarization) measured across the intercalant $L_{2,3}$ absorption edges (shown in the XAS measurements on the right of the panels) of $V_{1/3}\text{NbS}_2$, $\text{Cr}_{1/3}\text{NbS}_2$, and $\text{Fe}_{1/3}\text{NbS}_2$. (d) Experimental measures of the intercalant-derived PDOS of $V_{1/3}\text{NbS}_2$, $\text{Cr}_{1/3}\text{NbS}_2$, and $\text{Fe}_{1/3}\text{NbS}_2$, extracted from the difference between cuts of the on- and off-resonance spectra in (c). These are compared to the intercalant-derived PDOS calculated using DFT (see Section 2), for which a 200 meV broadening has been applied to simulate broadening from lifetime and experimental effects. The total areas under the curves have been normalized for clarity. (e) Direct comparison of the near Fermi level experimentally determined intercalant-derived PDOS shown in (d), normalized to the maximum measured intensity within the shown energy range. A trend of increasing intercalant-derived PDOS present at the Fermi level with increasing atomic number is observed across the materials studied.

However, evidence of stronger hybridizations between intercalant-derived local moment and Nb-derived itinerant states was reported in $\text{Cr}_{1/3}\text{NbS}_2$ and $\text{Co}_{1/3}\text{NbS}_2$,^{25–28} indicating that the simplest RKKY picture may not apply to all compounds in this material class, and pointing toward the choice of intercalant species playing a pivotal role in the electronic structure and nature of the magnetic interactions.

This is reflected in the disparate magnetic structures that are observed. In $V_{1/3}\text{NbS}_2$, the local V moments exhibit an A-type antiferromagnetic order, with an additional small canting of spins along the out-of-plane direction, which is reported to lead to a net uncompensated ferromagnetic moment.^{22,29} $\text{Cr}_{1/3}\text{NbS}_2$ instead hosts a chiral helimagnetic ground state,^{20,30,31} where a topologically protected chiral soliton lattice can be formed and modulated by an external magnetic field.^{21,32,33} In $\text{Fe}_{1/3}\text{NbS}_2$, the Fe sublattice orders antiferromagnetically,³⁴ with signatures of three-state nematicity,³⁵ and it has been shown to support current-induced magnetization switching at surprisingly low current densities.³⁶ Moreover, while the bulk magnetic properties of these compounds are well-studied, the magnetic phenomena at their termination-dependent surfaces—where markedly distinct charge transfer occurs—requires further exploration, as evident, for example, by the recent demonstration of a giant valley-Zeeman coupling in the NbS_2 surface layer of $V_{1/3}\text{NbS}_2$.³⁷

Here, we report a systematic study of the bulk and surface electronic structure of $V_{1/3}\text{NbS}_2$, $\text{Cr}_{1/3}\text{NbS}_2$, and $\text{Fe}_{1/3}\text{NbS}_2$ by combining resonant photoemission spectroscopy (ResPES)

and microscopic area spatially and angle-resolved photoemission spectroscopy (μ -ARPES) with density-functional theory (DFT) calculations. Our results demonstrate that intercalant-derived spectral weight is absent at the Fermi level of $V_{1/3}\text{NbS}_2$ but increasingly develops upon moving to the Cr- and Fe-based compounds, indicating the breakdown of a pure RKKY-like exchange mechanism. We show how these varying levels of hybridization lead to contrasting features in the surface-termination dependent electronic structures, with chemical potential variations that decrease with the increasing atomic number of the intercalant. Our results additionally allow us to identify the origin of the anomalous states reported at the Fermi level in this family of compounds,^{25,28,38–40} as the result of hybridizations between states derived from the electron-doped intercalant-terminated surface and subsurface NbS_2 layer.

2. METHODS

2.1. Crystal Growth. Single crystals of $M_{1/3}\text{NbS}_2$ ($M = \text{V}, \text{Cr},$ and Fe) were produced by the chemical vapor transport technique using iodine as the transport agent, as described previously.^{22,31} Presynthesized polycrystalline powders of the starting compositions, $M_{1/3}\text{NbS}_2$, along with ~ 5 mg/cm³ of the transport agent, were placed in an evacuated and sealed quartz tube. The tube was then heated with one end held at 950°C and the other at 800°C ($M = \text{Cr}$) or 850°C ($M = \text{V}$ and Fe) for 3 weeks before cooling to room temperature. Crystals in the form of platelets ranging from ~ 1 to 5 mm along their longest edges were formed. A backscattering X-ray Photonic-Science Laue camera system was used to assess the quality of the single crystals. Their composition was estimated by using

energy-dispersive X-ray spectroscopy analysis in a scanning electron microscope. Single crystal X-ray diffraction and transmission electron microscopy were used to confirm the noncentrosymmetric $P6_322$ space group adopted by these crystals for the critical composition of $M_{1/3}\text{NbS}_2$.^{22,31} In addition, we have confirmed the stoichiometry *via* measurements of the magnetic susceptibility, which for the Fe-based compound (see [Supplementary Figure 9](#)), is extremely sensitive to the precise stoichiometry achieved.³⁴

2.2. ResPES and XAS. Resonant photoemission spectroscopy (ResPES) and X-ray absorption spectroscopy (XAS) measurements were performed at the I09 beamline at Diamond Light Source using linear horizontal (LH) polarized light with photon energies between 507 and 729 eV and a beam spot size of $\sim 40 \times 20 \mu\text{m}^2$. The samples were cooled to a base temperature of ~ 27 K and cleaved *in situ* in a base pressure below 10^{-10} mbar. ResPES measurements were performed using a Scienta Omicron EW4000 analyzer, while XAS spectra were obtained from the sample drain currents in total electron yield mode. The partial density of states of the intercalant species was extracted by subtracting two photoemission spectra measured at photon energies on and just below the corresponding L_3 edge.

2.3. μ -ARPES and XPS. Microscopic area spatially and angle-resolved photoemission spectroscopy (μ -ARPES) and X-ray photoelectron spectroscopy (XPS) measurements were performed at the nano-ARPES branch of the I05 beamline at Diamond Light Source using linearly polarized light with photon energies between 79 and 200 eV and a beam spot size of $\sim 4 \times 4 \mu\text{m}^2$. The samples were mounted on a piezo-manipulator at a base temperature of ~ 35 K, cleaved *in situ* in a base pressure below 10^{-10} mbar, and measured using a Scienta Omicron DA30 analyzer. Additionally, the measurements of $\text{Cr}_{1/3}\text{NbS}_2$ presented in [Figure 3a,b](#) and [Supplementary Figure 4](#) were performed at the Bloch beamline at MAX IV Laboratory, at a base temperature of ~ 20 K, using a beam spot size of $\sim 10 \times 15 \mu\text{m}^2$.

2.4. DFT Calculations. The bulk electronic structure calculations were performed within density-functional theory (DFT) using the Perdew–Burke–Ernzerhof exchange–correlation functional⁴¹ and pseudopotential method as implemented in the Vienna Ab initio Simulation Package.^{42,43} Relativistic effects, including spin–orbit interactions, were fully taken into account. A $\sqrt{3} \times \sqrt{3} \times 1$ supercell containing six formula units of NbS_2 and two M atoms occupying the $(1/3, 2/3, 1/4)$ and $(2/3, 1/3, 3/4)$ intercalation sites, as shown in [Figure 1a](#), was used. The corresponding Brillouin zone was sampled using a $10 \times 10 \times 5$ k -mesh and plane-wave cutoff energy of 400 eV. For $M = \text{V}$ (Cr and Fe), an antiferromagnetic (ferromagnetic) ordering along $[001]$ was imposed. An additional on-site Hubbard term with an effective U value of $U_{\text{eff}} = 2$ eV (1 eV) was added to the $3d$ orbitals of the V and Fe (Cr) to reproduce the experimentally observed energetic alignment of the corresponding M states. We note that larger values of U did not lead to adequate agreement with our experimental measurements, establishing how the strong screening environment from the NbS_2 layers here leads to smaller U values than might otherwise be assumed for these $3d$ transition metals. Projected density of states calculations were performed by using a Wigner–Seitz radius of 1.3 Å for the intercalant ion and a Gaussian broadening factor of 200 meV to simulate the effect of lifetime broadening observed in the experiment. For the PDOS plots in [Figure 1](#), a Fermi–Dirac distribution was also applied to exclude states above the Fermi level.

For the surface structure calculations, a slab containing six units of $M_{1/3}\text{NbS}_2$ stacked along the crystalline c axis with a vacuum space of 12 Å was constructed. The corresponding Brillouin zone was sampled using a $8 \times 8 \times 1$ k -mesh. All other parameters were kept the same as those in the bulk calculations. The excess and depletion charge distribution shown in [Figure 4a,b](#) was obtained by computing the charge distribution for the entire slab, then subtracting the individual charge densities from the NbS_2 and Cr centers. The latter were obtained by removing Cr and NbS_2 layers in the same slab, respectively. The remaining was treated as excess whenever this

difference was positive, and as depletion whenever this difference was negative.

3. RESULTS

To gain an initial understanding of the impact of the intercalant species on the electronic structures of the three compounds discussed here, we first consider an approximation of their electronic configurations using crystal field theory. The trigonally distorted octahedral environment of the intercalated transition metal ions would be expected to split their d orbital energy levels as shown schematically in [Figure 1b](#).²⁴ In $\text{V}_{1/3}\text{NbS}_2$ and $\text{Cr}_{1/3}\text{NbS}_2$, the intercalants are expected to have a nominal +3 oxidation state,¹⁸ leading to a net donation of one electron from the intercalant layers to the NbS_2 layers (see [Figure 1a](#)). Two (three) electrons will thus fill the V (Cr) d orbital manifold in a high-spin configuration, as shown schematically in [Figure 1b](#), due to the relatively weak crystal field.²⁴ This simple picture is fully consistent with our bulk DFT calculations, where we find a local magnetic moment of $2 \mu_B$ ($3 \mu_B$) per V (Cr) ion, as well as our ResPES and XAS measurements for these compounds, shown in [Figure 1c](#). Extracting the intercalant-derived partial density of states (PDOS) from our ResPES measurements, as shown in [Figure 1d](#) (see also [Supplementary Figure 6](#)), we find a single broad PDOS contribution centered around 1 eV below the Fermi level for $\text{V}_{1/3}\text{NbS}_2$, which we attribute to the localized V-derived states nominally in the $d_{x^2-y^2}/d_{xy}$ orbitals. In comparison, a pronounced two-peak structure is observed in the Cr-derived PDOS, consistent with the higher d orbital population shown in [Figure 1b](#) (see also [Supplementary Figure 5](#) for a comparison between the intercalant-projected and total density of states). While our calculations do not quantitatively capture all features of our experimental measurements, such as an energy-dependent broadening due to lifetime effects that are beyond DFT, the agreement of the core features allows us to confidently assign chemical trends in the electronic structure, as discussed below.

In contrast to the V and Cr case, previous reports²⁴ indicate that $\text{Fe}_{1/3}\text{NbS}_2$ hosts the intercalated Fe ions in +2 oxidation states. This will lower the net charge transfer from the Fe to the NbS_2 layers ([Figure 1a](#)) and will lead to a nominal $3d^6$ electron configuration of the Fe sites. The crystal field is still expected to be relatively weak,²⁴ and so a high-spin configuration can still be expected, as shown in [Figure 1b](#). Consistent with this, a broad distribution of Fe-derived PDOS is found throughout the valence band in both our ResPES measurements and our corresponding DFT calculations. Our calculations also reveal that each Fe effectively maintains a local magnetic moment of $3.6 \mu_B$, further confirming its distinctive 2+ ionic state in this group of compounds. Interestingly, we find that the resulting Fe-derived spectral weight persists right up to the Fermi level, with the intercalant-derived PDOS at the Fermi level showing a systematic increase with an increasing atomic number of the intercalated transition metal in both our calculated and experimentally determined intercalant-derived PDOS ([Figure 1d,e](#)).

The simplest picture of the metal-intercalated TMDs assumes that the intercalant atoms act as local moments, otherwise modifying the electronic structure of NbS_2 purely *via* electron doping in a rigid band shift picture,^{18,19} with the magnetic interactions described within an RKKY picture. While our measurements here show that this picture remains

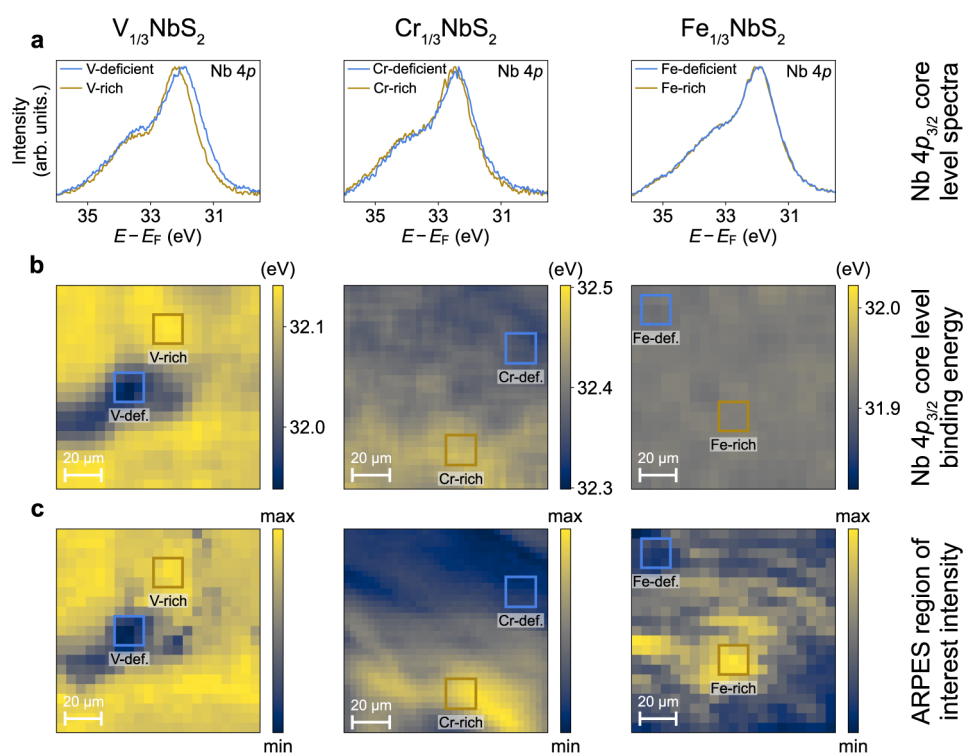


Figure 2. Spatial mapping of $M_{1/3}\text{NbS}_2$ compounds. (a) Representative Nb $4p$ core-level spectra ($h\nu = 200$ eV, LH polarization) of the intercalant-deficient (blue) and intercalant-rich (brown) surface terminations of $V_{1/3}\text{NbS}_2$ ($T = 32$ K), $\text{Cr}_{1/3}\text{NbS}_2$ ($T = 35$ K), and $\text{Fe}_{1/3}\text{NbS}_2$ ($T = 43$ K), extracted from the regions of spatial mapping data indicated in (b). (b) Spatial maps displaying the fitted binding energies of the Nb $4p_{3/2}$ core levels of $V_{1/3}\text{NbS}_2$, $\text{Cr}_{1/3}\text{NbS}_2$, and $\text{Fe}_{1/3}\text{NbS}_2$. To allow for a comparison of the intercalant-dependent binding energy shifts, the maps were plotted using color scales with the same size binding energy range. (c) Spatial maps (LH polarization) of $V_{1/3}\text{NbS}_2$ ($T = 33$ K, $h\nu = 79$ eV), $\text{Cr}_{1/3}\text{NbS}_2$ ($T = 35$ K, $h\nu = 100$ eV), and $\text{Fe}_{1/3}\text{NbS}_2$ ($T = 36$ K, $h\nu = 80$ eV) displaying the integrated spectral weight within the region of interest of ARPES measurements of the low-energy electronic structure corresponding to intercalant-derived states (see [Supplementary Figure 1](#) for more information). High (yellow) and low (blue) intensity regions correspond to the intercalant-rich and intercalant-deficient surface terminations, respectively.

approximately valid for the V cations, it increasingly breaks down for Cr and Fe, instead pointing to a more complex interplay between the local moment and itinerant states (see also [Supplementary Figure 8](#)). Indeed, given that conduction in these compounds is largely governed by Nb $4d$ -derived orbitals, the presence of intercalant-derived weight at the Fermi level points to stronger hybridizations between local moment intercalant-derived and itinerant Nb-derived states. For the Fe-based compound, in particular, the strong intercalant-derived weight at the Fermi level and broad bandwidth of Fe-derived states points to a strong hybridization between the intercalant- and NbS_2 -derived states, leading to a collapse of the rigid band shift picture, similar to the conclusions recently drawn from studies of $\text{Co}_{1/3}\text{NbS}_2$.^{27,28} The Cr-based material appears intermediate between these regimes,²⁵ and we thus conclude that there is a strong and approximately monotonic chemical trend of increasing hybridization tied to the increasing atomic number of the intercalated metal species here, which can in turn be expected to dominate the magnetic interactions in these compounds.

To investigate these electronic structure trends in more detail, we performed k -resolved electronic structure measurements using ARPES. A significant complication, however, is that the interlayer charge transfer discussed above becomes strongly modified at the surface of such materials.^{37,40,44,45} ARPES, in particular, when performed at the photon energies

used here, is a highly surface-sensitive technique. It is thus this distinct surface electronic structure that will be probed. Furthermore, due to the natural cleavage plane being situated between the intercalant and NbS_2 layers, both intercalant-exposed and NbS_2 -exposed surface terminations can be expected. Indeed, such distinct terminations have previously been observed in STM measurements over a field of view of ~ 100 nm.³⁸ Moreover, spectromicroscopy has shown that such regions are randomly distributed across the surface, with characteristic variations observed at the few-micron scale.³⁷ Additional factors relating to crystallographic defects, such as polycrystalline structures, stacking faults, or the presence of multiple polymorphs, would also lead to variations of the surface at the mesoscopic level. In the following, however, we consider that spatial variations in the surface terminations are the key differentiating feature.

To enable probing of different surface terminations, we thus performed ARPES measurements using a focused light source (μ -ARPES, see [Section 2](#)). To identify the unique surface terminations of $V_{1/3}\text{NbS}_2$, $\text{Cr}_{1/3}\text{NbS}_2$, and $\text{Fe}_{1/3}\text{NbS}_2$, we initially performed spectromicroscopy measurements using photoemission of the Nb $4p$ core level (see [Figure 2a](#)). A 200 eV photon energy was used for these measurements, providing sufficient surface sensitivity to characterize the distinct surface terminations.

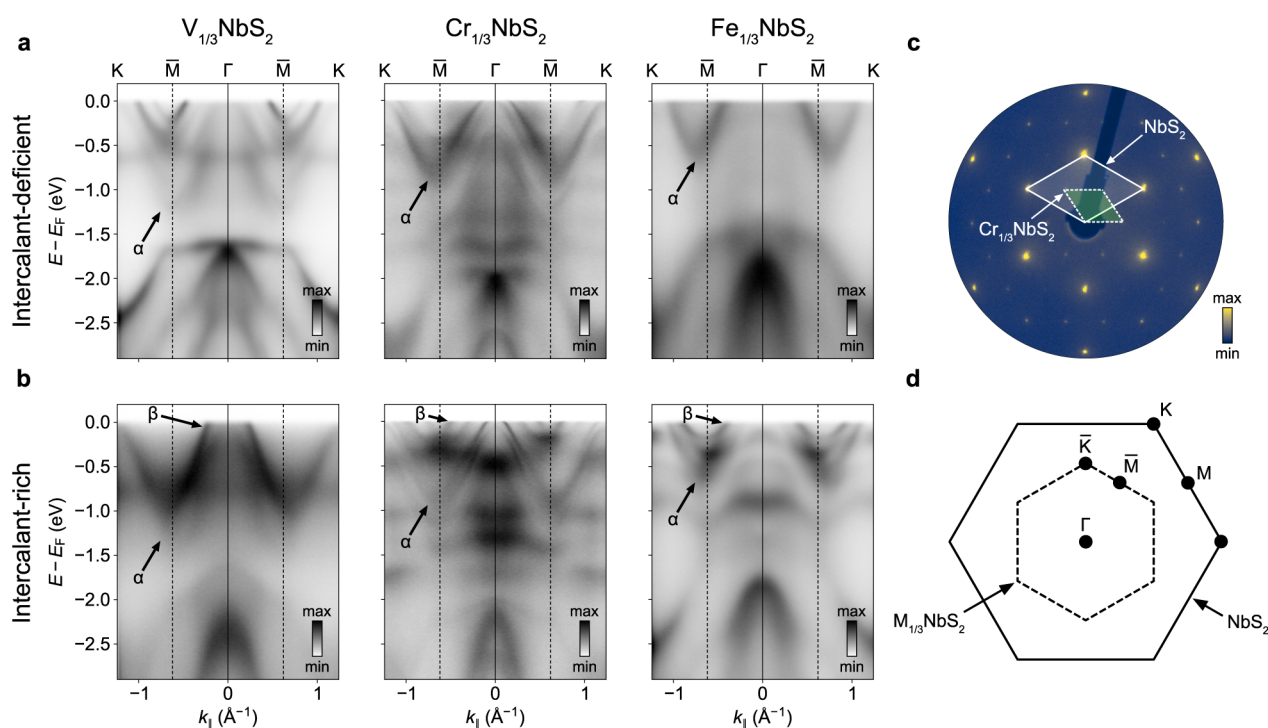


Figure 3. Surface termination-dependent electronic structure of $M_{1/3}\text{NbS}_2$ compounds. (a,b) ARPES dispersions along Γ -K ($h\nu = 79$ eV, LH polarization) of the (a) intercalant-deficient and (b) intercalant-rich surface terminations of $V_{1/3}\text{NbS}_2$ ($T = 33$ K), $\text{Cr}_{1/3}\text{NbS}_2$ ($T = 20$ K), and $\text{Fe}_{1/3}\text{NbS}_2$ ($T = 38$ K). States labeled α and β are bulk- and surface-derived, respectively. (c) LEED image of $\text{Cr}_{1/3}\text{NbS}_2$ measured using a 220 eV electron energy ($T = 14$ K) demonstrating how the intercalants generate the reduced and rotated Brillouin zone shown in (d). The reciprocal space unit cells of the NbS_2 and $\text{Cr}_{1/3}\text{NbS}_2$ lattices are indicated. (d) Schematic of the Brillouin zones of NbS_2 and $M_{1/3}\text{NbS}_2$ at $k_z = 0$. A reduced and rotated Brillouin zone is observed in $M_{1/3}\text{NbS}_2$ compared to NbS_2 , generated by the $\sqrt{3} \times \sqrt{3} R30^\circ$ superstructure of intercalant atoms. The high symmetry points of the $M_{1/3}\text{NbS}_2$ Brillouin zone are labeled with overbars. Backfolding of some states around the reduced Brillouin zone boundaries is evident in (a,b), indicated by the dashed lines.

To analyze the spatial variations of the Nb $4p$ core level, we fit the peaks of the spectra across the spatial mapping region and show the spatial dependence of the Nb $4p_{3/2}$ binding energy in Figure 2b. Considering first the case of $V_{1/3}\text{NbS}_2$, we observe the emergence of distinct regions in the spatial map, with areas of decreased (increased) binding energy of the core level, with shifts visible on the order of 200 meV (see also Figure 2a). These correspond to chemical potential variations that result from decreased (increased) electron doping of the surface region. We assign the former regions to intercalant-deficient surface terminations hosting significant concentrations of exposed NbS_2 surface layers and low concentrations of surface intercalants. Here, the absence of electron donation into the surface NbS_2 layer from the missing intercalant atoms atop results in an effective hole-like self-doping of the surface layer. In contrast, we assign the more electron-doped regions to intercalant-rich surface terminations, where the previously intercalated atoms are now effectively adsorbed on the sample surface. The missing NbS_2 layers above such a surface plane can no longer act as electron acceptors, leading to an electron-like self-doping of the intercalant-terminated surface layer.

While the distinct spatial regions are sharply defined for the V-based compound in Figure 2b, with corresponding pronounced changes in the core level spectra (Figure 2a), more subtle variations are observed across the surface of the Cr-based compound. The lack of variation becomes even more extreme in the Fe-based compound, where negligible contrast is observed beyond the experimental noise. Nonetheless,

unique surface terminations can still also be reliably identified by performing spectromicroscopy of the low-energy electronic structure using ARPES, as shown in Figure 2c where the integrated spectral weight within the region of interest corresponding to intercalant-derived states associated with the intercalant-rich surface terminations is shown (see Supplementary Figures 1 and 2). We suggest that the reduced chemical potential variations seen in the Nb $4p_{3/2}$ binding energy spatial maps of $\text{Cr}_{1/3}\text{NbS}_2$ and $\text{Fe}_{1/3}\text{NbS}_2$ in Figure 2b are the result of increased hybridizations with the intercalant species in these compounds, as compared to $V_{1/3}\text{NbS}_2$ (as identified above). This would result in a reduced ionic charge transfer from the intercalant to the NbS_2 layer, making the termination-dependent core level spectral changes less clear, while also leading to a stronger bonding between the intercalant and the NbS_2 layers and thus producing a less natural cleavage plane in the material. We would therefore expect smaller areas of distinct surface termination and thus increased regions probed with mixed terminations, making the spatial variation less clear in the Cr- and Fe-based compounds, entirely consistent with our measurements in Figure 2. In this respect, we note that previous scanning tunneling microscopy studies have observed locally rather disordered terminations for the Cr-terminated surface of $\text{Cr}_{1/3}\text{NbS}_2$,³⁸ again supporting this picture. We therefore refer here to intercalant-rich and intercalant-deficient terminations rather than assigning these as pure and clean surface terminations.

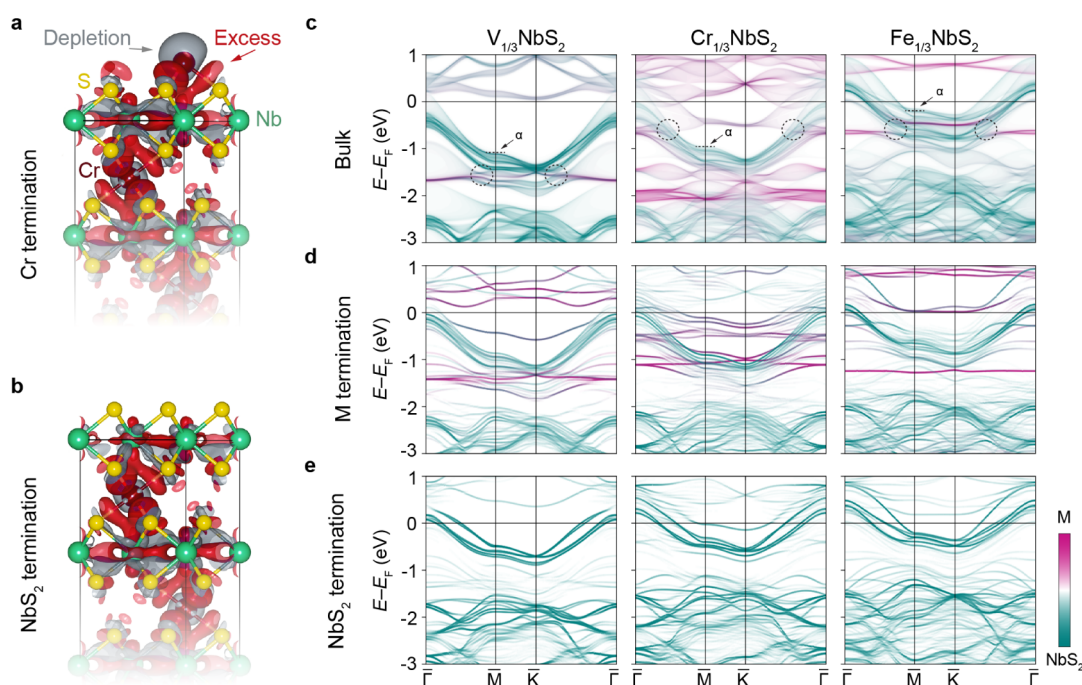


Figure 4. Calculated bulk and surface-termination dependent electronic structure of $M_{1/3}\text{NbS}_2$ compounds. (a,b) Computed excess-depletion charge density distribution for the intermediate case of $\text{Cr}_{1/3}\text{NbS}_2$ for the (a) intercalant and (b) NbS_2 surface terminations. Here, the excess (depletion) charge is defined as the effective charge added (subtracted) to (from) the pristine NbS_2 lattice due to Cr intercalation. (c) Site-projected bulk electronic structure of $\text{V}_{1/3}\text{NbS}_2$, $\text{Cr}_{1/3}\text{NbS}_2$, and $\text{Fe}_{1/3}\text{NbS}_2$ integrated over all k_z values along a high symmetry path in the reduced Brillouin zone. Here, α denotes the upper edge of the topmost NbS_2 -derived valence band in each compound. The dashed circles indicate the typical regions where orbital mixing between the intercalant- and NbS_2 -derived states leads to a series of hybridization gaps, appearing as abrupt discontinuities in the energy dispersions of the involved states. (d,e) The corresponding surface electronic structures projected onto the (d) intercalant and (e) NbS_2 terminations.

Having identified areas of at least dominantly distinct terminations, we turn to the corresponding electronic structures. We summarize these in Figure 3a,b. These measurements were performed along the Γ -K direction of the NbS_2 lattice surface Brillouin zone. However, as shown in the low-energy electron diffraction (LEED) image and Brillouin zone schematic in Figure 3c,d, the $\sqrt{3} \times \sqrt{3} R30^\circ$ intercalant superlattice periodicity will give rise to a reduced and rotated Brillouin zone in $M_{1/3}\text{NbS}_2$ compounds. Signatures of this reduced zone can be seen by inspecting the dispersions in Figure 3a,b, where a backfolding of some states around the reduced Brillouin zone boundary (\bar{M} point, indicated by a dashed line) is evident. In all of the measured surface termination-dependent electronic structures, we observe two manifolds of highly dispersive bands. From comparison to the electronic structure of 2H-NbS_2 ,^{46,47} we conclude that the states below ~ 1.5 eV are dominantly S-derived, while the dispersive states in the vicinity of the Fermi level are mostly Nb 4d-derived.

Detailed interpretation of the electronic structures is, however, made more challenging by the presence of spectral signatures of both surface and bulk states in our measurements, with the former resulting from the distinct surface environment. Comparing the variations seen in the two surface terminations of the compounds, we assign the states labeled α in Figure 3a,b as the bulk Nb-derived conduction bands. These states are located at distinct binding energies for the different intercalant species, pointing to a significant variation in interlayer charge transfer in these compounds. Indeed, in $\text{V}_{1/3}\text{NbS}_2$ and $\text{Cr}_{1/3}\text{NbS}_2$, the +3 oxidation states of the

intercalants are seen to give rise to more heavily electron-doped Nb-derived α bands, as compared to in $\text{Fe}_{1/3}\text{NbS}_2$ where the Fe intercalants only have a +2 oxidation state. Furthermore, the Nb-derived α band in $\text{Cr}_{1/3}\text{NbS}_2$ can be seen to be less electron-doped than in $\text{V}_{1/3}\text{NbS}_2$. Consistent with our ResPES measurements, this points to a deviation away from an ionic-like charge transfer picture in $\text{Cr}_{1/3}\text{NbS}_2$, with stronger hybridizations between intercalant and NbS_2 layers than in $\text{V}_{1/3}\text{NbS}_2$ instead being present, giving rise to a reduced occupied bandwidth.

An additional feature of the low-energy electronic structures is the presence of flatter, and thus more localized, states, which we assign as intercalant-derived. Consistent with our surface termination assignments, these states become more intense on the intercalant-rich surface terminations shown in Figure 3b. The electronic structures presented here thus provide insights into the results of intercalant-specific PDOS obtained from our ResPES measurements. Indeed, in $\text{V}_{1/3}\text{NbS}_2$, the lowest binding energy localized V-derived state we observe is positioned relatively far from the Fermi level at ~ 0.8 eV (consistent with our ResPES results in Figure 1d) and shows little sign of hybridization with the dispersive NbS_2 -derived states, remaining largely dispersionless. From such an electronic structure, we would expect minimal V-derived spectral weight at the Fermi level, consistent with our ResPES measurements and an RKKY-mediated mechanism of the magnetism in $\text{V}_{1/3}\text{NbS}_2$. In contrast, in $\text{Cr}_{1/3}\text{NbS}_2$, localized Cr-derived states are present much closer to the Fermi level, and hybridizations with the itinerant Nb-derived states are

evident by spectral weight transfers from Cr- to Nb-derived states. In particular, the Cr-derived state at a binding energy of ~ 0.4 eV develops a noticeable dispersion, particularly evident for the Cr-rich surface termination, providing further evidence of the hybridization between localized and itinerant states and leading to Cr-derived weight in the vicinity of the Fermi level, consistent with our ResPES measurements and PDOS calculations in Figure 1d. For the Fe-based compound, localized intercalant-derived states are positioned even closer to the Fermi level. Here, yet stronger hybridizations between intercalant- and Nb-derived states are evident, where the flatter intercalant-derived states are seen to develop considerable dispersion, and hybridization gaps resulting from avoided crossings with the Nb-derived states are observed. This gives rise to the strong Fe-derived spectral weight at the Fermi level shown in Figure 1d. As such, an RKKY picture of magnetism in $\text{Cr}_{1/3}\text{NbS}_2$ and $\text{Fe}_{1/3}\text{NbS}_2$ can be conclusively ruled out, instead pointing towards mechanisms involving substantial hybridizations between intercalant- and Nb-derived states, such as a previously suggested Hund's coupling.²⁵

By comparing the dispersions of the intercalant-deficient surface terminations shown in Figure 3a to the intercalant-rich surface terminations in Figure 3b, a general trend of a more complex near-Fermi level electronic structure with more states visible on the intercalant-rich surface terminations is observed. We label these new dispersive states as β . Similar states have been observed previously in the $\text{M}_{1/3}\text{NbS}_2$ class of materials, with their origin being the topic of considerable debate.^{25,28,38–40} Such states are inconsistent with the bulk electronic structure (Figure 4c). Given the strong termination-dependent changes evident here, we thus consider their origin as arising from the polar surfaces of these compounds.

On a pure NbS_2 -exposed surface termination, the absence of an intercalant layer above can be expected to generate hole-doped surface-derived analogues of the bulk NbS_2 states, as demonstrated in our previous work on $\text{V}_{1/3}\text{NbS}_2$.³⁷ Indeed, such states can be seen above the α band in Figure 3a for the intercalant-deficient surface termination of $\text{V}_{1/3}\text{NbS}_2$. Equivalent states are not clearly observed on the intercalant-deficient surface termination of $\text{Cr}_{1/3}\text{NbS}_2$ and $\text{Fe}_{1/3}\text{NbS}_2$, likely due to a larger presence of disordered intercalants at the surface in these compounds than on the V-based compound, giving rise to a broadening and reduction in spectral weight of any surface states. That such clean NbS_2 -exposed surface terminations are only observed for $\text{V}_{1/3}\text{NbS}_2$ is consistent with the weaker bonding between NbS_2 and intercalant layers discussed above than for the Cr- and Fe-based compounds, resulting in a more natural cleave plane. However, as the intercalant concentration increases, the surface can be expected to become more ordered, leading to the emergence of the visible surface states labeled as β in Figure 3b.

To gain a more comprehensive understanding of these electronic states, we conducted systematic bulk and surface electronic structure calculations. In Figure 4a,b, we present the excess-depletion charge density distributions of $\text{Cr}_{1/3}\text{NbS}_2$ for the intercalant and NbS_2 surface terminations, respectively. Such a picture is typical for all three compounds studied. The intercalant ions inject a significant charge into the van der Waals gap between neighboring NbS_2 layers, intensifying interlayer bonding. Crucially, this facilitates effective magnetic exchange interactions between the intercalant sites across the NbS_2 layers. In contrast, charge density within the NbS_2 layers

experiences partial depletion, indicating that the Nb ion, in the presence of the M intercalant, partially regains its nominal 3+ oxidation state, deviating from the pristine NbS_2 compound's 4+ state. At the surface terminations, a noticeable distinction emerges. While the NbS_2 surface terminations appear to only be minimally affected for the Cr-derived case shown here, the intercalant surface termination accumulates the maximum charge compared to the underlying layers. Consequently, the NbS_2 states on the M-terminated side are expected to be maximally electron-doped, leading to a downward shift within the overall energy spectrum. Furthermore, the intercalant surface termination ensures a significant contribution of the intercalant 3d orbitals to the electronic structure.

Despite the apparent similarities of the different $\text{M}_{1/3}\text{NbS}_2$ compounds in real space, a profound disparity arises in their momentum space. In Figure 4c and Supplementary Figure 7, we present a comparison of the calculated site-projected bulk electronic structures for $\text{V}_{1/3}\text{NbS}_2$, $\text{Cr}_{1/3}\text{NbS}_2$, and $\text{Fe}_{1/3}\text{NbS}_2$. Moving from V to Fe, we can see escalating alterations in the electronic dispersions of the host NbS_2 bands due to the influence of the intercalant 3d orbitals. In $\text{V}_{1/3}\text{NbS}_2$, V-derived states primarily contribute as nonbonding flat bands residing at a binding energy of ~ 1.5 eV, slightly overlapping with the lower edge of the NbS_2 -derived valence bands. Consequently, the resulting electronic structure bears a resemblance to that of pristine NbS_2 . Consistent with our above discussions, this suggests that any magnetic alignment between V ions can only be stabilized through indirect exchange coupling processes, such as the RKKY interaction, facilitated by charge carriers at the Fermi level. In contrast, the Cr 3d orbitals in $\text{Cr}_{1/3}\text{NbS}_2$ have a higher filling number compared to the V case, and thus exhibit a more substantial presence at and below the Fermi level, effectively hybridizing with the topmost NbS_2 -derived bands and giving rise to additional dispersive bands over a wide energy range. This implies a more inherently itinerant form of magnetism in $\text{Cr}_{1/3}\text{NbS}_2$, a conclusion supported by our ResPES and ARPES measurements. The situation becomes even more pivotal in $\text{Fe}_{1/3}\text{NbS}_2$, where the Fe states significantly modify the electronic structure away from the picture of pristine NbS_2 . The preference of Fe to maintain its 3d⁶ state allows its 3d orbitals to reside at energies considerably below the Fermi level, enabling robust hybridization with both S 3p and Nb 4d states (Supplementary Notes 4 and 5 and the associated figures present a comparative analysis of intercalant hybridization and its effect on host electronic states in $\text{M}_{1/3}\text{NbS}_2$). This leads to a broadened bandwidth for the entire bulk valence continuum and an upward shift of the original topmost NbS_2 bands, as is evident in Figure 4c.

Figure 4d,e shows the surface electronic structures for the intercalant and NbS_2 surface terminations, respectively. Moving from V to Fe, we can again see a noticeable overall shift of the bands toward lower binding energies for both terminations. This shift, as explained above, is attributed to the significant enhancement of hybridizations between intercalant 3d orbitals and host NbS_2 states in $\text{Cr}_{1/3}\text{NbS}_2$ and $\text{Fe}_{1/3}\text{NbS}_2$ compared to $\text{V}_{1/3}\text{NbS}_2$, with $\text{Fe}_{1/3}\text{NbS}_2$ exhibiting the most pronounced electronic structure modification. Comparison of the two terminations illustrates a consistently deeper energy spectrum for the intercalant surface terminations across all three compounds. This finding aligns with our excess-depletion

charge density calculations: while the subsurface NbS₂ layer can now be expected to retain close to its bulk-like configuration, with charge transfer from intercalant layers above and below, the surface intercalant layer will now become electron-doped due to the absence of a NbS₂ layer above, giving rise to the β states observed experimentally. For the NbS₂ surface terminations (Figure 4e), the intercalants here lack direct contributions to the energy bands. Nevertheless, they indirectly influence the details of the band dispersions, particularly at and near the Fermi level, owing to their spatial and energetic proximities to these bands. Thus, these surface terminations serve as an ideal medium for creating magnetically controllable carriers with rich valleytronic properties.³⁷

In contrast, for the intercalant surface terminations shown in Figure 4d, a distinct disparity in the formation of intercalant-derived bands near the Fermi level becomes evident. While V_{1/3}NbS₂ displays a single flat intercalant-dominated band in the occupied electronic structure, at a binding energy of ~ 0.5 eV, Cr_{1/3}NbS₂ instead possesses a ladder of such bands spanning a ~ 1 eV energy window below the Fermi level. In Fe_{1/3}NbS₂, a well-localized flat band is located at 1 eV binding energy, while additional significant intercalant-derived spectral weight is visible in the vicinity of the Fermi level and also at deeper binding energy (Supplementary Figure 7). The bands sitting just at the Fermi level are likely slightly occupied in the experimental measurements, leading to the complex electronic structure near the Fermi level observed in Figure 3b. These evidently have a mixed Nb–Fe character, enabling their dispersion down to the Fermi level, and their population in the electron-doped surface layer.

While these new β states are derived from the intercalant-terminated surfaces, their mixed atomic character is clear from their significant dispersion, evident in both our measured dispersions and Fermi maps (see Supplementary Figure 3). Indeed, their dispersive nature has led to some challenges in assigning these states. In particular, in Cr_{1/3}NbS₂, the presence of the β bands at the Fermi level has been of significant attention, with splittings in these attributed to an exchange splitting in the low-energy electronic structure of Cr_{1/3}NbS₂.^{25,48} However, as discussed in Supplementary Note 3, with the new understanding of surface- and bulk-derived states advanced here, we can now rule out the possibility that the observed temperature-dependent changes are related to any resolvable exchange splitting of itinerant Nb-derived states.

4. CONCLUSIONS

Our measurements on V_{1/3}NbS₂, Cr_{1/3}NbS₂, and Fe_{1/3}NbS₂, and corresponding DFT calculations, have demonstrated a pronounced and element-specific role of the intercalants on the electronic structure of metal-intercalated TMDs. In all three compounds, marked differences were observed in the electronic structure as compared to those of 2H-NbS₂. These include electron doping of bands from interlayer charge transfers and the backfolding of bands around the reduced Brillouin zone boundaries that are generated by the intercalant superlattices. Furthermore, shifts in the chemical potential that arise from self-doping at polar surfaces led to distinct surface terminations in these compounds. It was additionally shown that the choice of intercalant species leads to varying amounts of hybridizations between localized intercalant- and itinerant Nb-derived states, resulting in nontrivial differences between the electronic structure of these compounds. Indeed, the

minimal hybridizations in V_{1/3}NbS₂ lead to a scenario where the effect of the intercalant is well-described by the ionic-like charge transfers of a rigid band shift picture, in turn facilitating RKKY-mediated magnetic interactions. In contrast, stronger interlayer hybridizations in Cr_{1/3}NbS₂ and Fe_{1/3}NbS₂ mean that the localized intercalant-derived states are no longer weakly coupled to the itinerant Nb-derived states. As such, an RKKY-like exchange mechanism is insufficient to describe the magnetic interactions in these two compounds, motivating further investigations into the origin of their magnetic order. Furthermore, we provided an explanation for the origin of the anomalous states frequently reported at the Fermi level in the M_{1/3}NbS₂ compounds, as the result of hybridizations between electron-doped surface intercalant-derived and subsurface NbS₂-derived states. This assignment allowed us to rule out the possibility of a previously reported exchange splitting of the Nb 4*d*-derived conduction bands at the surface of Cr_{1/3}NbS₂. Together, our combined experimental and theoretical study has identified how systematic changes in the orbital filling and ionicity of the intercalants in M_{1/3}NbS₂ contribute to the creation of magnetically rich surfaces with distinct electronic properties, opening new prospects for tuning these *via* materials design.

■ ASSOCIATED CONTENT

Data Availability Statement

The research data supporting this publication can be accessed at [10.17630/295fc754-5305-461c-9640-557cd304de81](https://doi.org/10.17630/295fc754-5305-461c-9640-557cd304de81).⁴⁹

Supporting Information

The Supporting Information is available free of charge at <https://pubs.acs.org/doi/10.1021/acs.chemmater.4c00824>.

Supplementary notes providing additional discussion of (1) spatial mapping photoemission data analysis, (2) Fermi surface measurements, (3) temperature-dependent ARPES measurements of Cr_{1/3}NbS₂, (4) calculated densities of states, and (5) chemical trends in the degree of electronic hybridization. Supplementary figures of (1,2) spatial mapping ARPES data, (3) Fermi surface measurements, (4) temperature-dependent ARPES, (5) density of states calculations, (6) resonant photoemission measurements, (7,8) calculated bulk electronic structures and spin densities, and (9) magnetic characterization (PDF)

■ AUTHOR INFORMATION

Corresponding Authors

Mohammad Saeed Bahramy – Department of Physics and Astronomy, University of Manchester, Manchester M13 9PL, U.K.; orcid.org/0000-0001-9024-6335; Email: m.saeed.bahramy@manchester.ac.uk

Phil D. C. King – SUPA, School of Physics and Astronomy, University of St Andrews, St Andrews KY16 9SS, U.K.; orcid.org/0000-0002-6523-9034; Email: pdk6@st-andrews.ac.uk

Authors

Brendan Edwards – SUPA, School of Physics and Astronomy, University of St Andrews, St Andrews KY16 9SS, U.K.; orcid.org/0000-0002-7219-4241

Darius-A. Deaconu – Department of Physics and Astronomy, University of Manchester, Manchester M13 9PL, U.K.; orcid.org/0000-0002-5698-0728

Philip A. E. Murgatroyd – SUPA, School of Physics and Astronomy, University of St Andrews, St Andrews KY16 9SS, U.K.

Sebastian Buchberger – SUPA, School of Physics and Astronomy, University of St Andrews, St Andrews KY16 9SS, U.K.; Max Planck Institute for Chemical Physics of Solids, Dresden 01187, Germany

Tommaso Antonelli – SUPA, School of Physics and Astronomy, University of St Andrews, St Andrews KY16 9SS, U.K.

Daniel Halliday – SUPA, School of Physics and Astronomy, University of St Andrews, St Andrews KY16 9SS, U.K.; Diamond Light Source Ltd, Didcot OX11 0DE, U.K.

Gesa-R. Siemann – SUPA, School of Physics and Astronomy, University of St Andrews, St Andrews KY16 9SS, U.K.; orcid.org/0000-0003-0029-5059

Andela Zivanovic – SUPA, School of Physics and Astronomy, University of St Andrews, St Andrews KY16 9SS, U.K.; Max Planck Institute for Chemical Physics of Solids, Dresden 01187, Germany

Liam Trzaska – SUPA, School of Physics and Astronomy, University of St Andrews, St Andrews KY16 9SS, U.K.

Akhil Rajan – SUPA, School of Physics and Astronomy, University of St Andrews, St Andrews KY16 9SS, U.K.; orcid.org/0000-0001-5356-3032

Edgar Abarca Morales – SUPA, School of Physics and Astronomy, University of St Andrews, St Andrews KY16 9SS, U.K.; Max Planck Institute for Chemical Physics of Solids, Dresden 01187, Germany

Daniel A. Mayoh – Department of Physics, University of Warwick, Coventry CV4 7AL, U.K.; orcid.org/0000-0002-7020-3263

Amelia E. Hall – Department of Physics, University of Warwick, Coventry CV4 7AL, U.K.

Rodion V. Belosludov – Institute for Materials Research, Tohoku University, Sendai 980-08577, Japan; orcid.org/0000-0003-4661-9194

Matthew D. Watson – Diamond Light Source Ltd, Didcot OX11 0DE, U.K.

Timur K. Kim – Diamond Light Source Ltd, Didcot OX11 0DE, U.K.; orcid.org/0000-0003-4201-4462

Deepnarayan Biswas – Diamond Light Source Ltd, Didcot OX11 0DE, U.K.

Tien-Lin Lee – Diamond Light Source Ltd, Didcot OX11 0DE, U.K.

Craig M. Polley – MAX IV Laboratory, Lund University, Lund 221 00, Sweden

Dina Carbone – MAX IV Laboratory, Lund University, Lund 221 00, Sweden

Mats Leandersson – MAX IV Laboratory, Lund University, Lund 221 00, Sweden

Geetha Balakrishnan – Department of Physics, University of Warwick, Coventry CV4 7AL, U.K.

Complete contact information is available at: <https://pubs.acs.org/10.1021/acs.chemmater.4c00824>

Notes

The authors declare no competing financial interest.

ACKNOWLEDGMENTS

We thank T. Balasubramanian for useful discussions. We gratefully acknowledge support from the Leverhulme Trust (Grant Nos. RL-2016-006 and RPG-2023-253), the European Research Council (through the QUESTDO project, 714193), and the Engineering and Physical Sciences Research Council (Grant Nos. EP/T02108X/1, EP/T005963/1 and EP/N032128/1). S.B., A.Z., and E.A.M. gratefully acknowledge studentship support from the International Max-Planck Research School for Chemistry and Physics of Quantum Materials. D.-A.D. had support from EPSRC CDT Graphene NOWNANO, grant EP/L01548X/1. We gratefully acknowledge Diamond Light Source for access to the I09 (Proposal No. SI32937-1) and I05 (Proposal Nos. SI30125-1b and SI31465-1) beamlines, as well as MAX IV Laboratory for time on the Bloch beamline (Proposal Nos. 20210091 and 20210763), which all contributed to the results presented here. We also gratefully acknowledge the Center for Computational Materials Science at the Institute for Materials Research for allocations on the MASAMUNE-IMR supercomputer system (Project No. 202112-SCKXX-0510). Research conducted at MAX IV Laboratory, a Swedish national user facility, is supported by the Swedish Research Council under contract 2018-07152, the Swedish Governmental Agency for Innovation Systems under contract 2018-04969, and Formas under contract 2019-02496. The research leading to this result has been supported by the project CALIPSOplus under the Grant Agreement 730872 from the EU Framework Programme for Research and Innovation HORIZON 2020. For the purpose of open access, the authors have applied a Creative Commons Attribution (CC BY) licence to any author accepted manuscript version arising.

REFERENCES

- (1) Choi, W.; et al. Recent development of two-dimensional transition metal dichalcogenides and their applications. *Mater. Today* **2017**, *20*, 116–130.
- (2) Novoselov, K. S.; Mishchenko, A.; Carvalho, A.; Neto, A. H. C. 2D materials and van der Waals heterostructures. *Science* **2016**, *353* (6298), aac9439.
- (3) Manzeli, S.; Ovchinnikov, D.; Pasquier, D.; Yazyev, O. V.; Kis, A. 2D transition metal dichalcogenides. *Nat. Rev. Mater.* **2017**, *2* (8), 17033.
- (4) Chhowalla, M.; et al. The chemistry of two-dimensional layered transition metal dichalcogenide nanosheets. *Nat. Chem.* **2013**, *5*, 263–275.
- (5) Cao, T.; et al. Valley-selective circular dichroism of monolayer molybdenum disulphide. *Nat. Commun.* **2012**, *3* (1), 887.
- (6) Mak, K. F.; He, K.; Shan, J.; Heinz, T. F. Control of valley polarization in monolayer MoS₂ by optical helicity. *Nat. Nanotechnol.* **2012**, *7*, 494–498.
- (7) Zeng, H.; Dai, J.; Yao, W.; Xiao, D.; Cui, X. Valley polarization in MoS₂ monolayers by optical pumping. *Nat. Nanotechnol.* **2012**, *7*, 490–493.
- (8) Riley, J. M.; et al. Direct observation of spin-polarized bulk bands in an inversion-symmetric semiconductor. *Nat. Phys.* **2014**, *10*, 835–839.
- (9) Bawden, L.; et al. Spin–valley locking in the normal state of a transition-metal dichalcogenide superconductor. *Nat. Commun.* **2016**, *7* (1), 11711.
- (10) Wilson, J. A.; Di Salvo, F. J.; Mahajan, S. Charge-density waves in metallic, layered, transition-metal dichalcogenides. *Phys. Rev. Lett.* **1974**, *32*, 882–885.
- (11) Morosan, E.; et al. Superconductivity in Cu_xTiSe₂. *Nat. Phys.* **2006**, *2*, 544–550.

- (12) Kusmartseva, A. F.; Sipos, B.; Berger, H.; Forro, L.; Tutiš, E. Pressure induced superconductivity in pristine 1T-TiSe₂. *Phys. Rev. Lett.* **2009**, *103*, 236401.
- (13) Feng, J.; et al. Electronic structure and enhanced charge-density wave order of monolayer VSe₂. *Nano Lett.* **2018**, *18*, 4493–4499.
- (14) Antonelli, T.; et al. Controlling the charge density wave transition in single-layer ys by band gap engineering. *Nano Lett.* **2024**, *24*, 215–221.
- (15) Qian, X.; Liu, J.; Fu, L.; Li, J. Quantum spin hall effect in two-dimensional transition metal dichalcogenides. *Science* **2014**, *346*, 1344–1347.
- (16) Bahramy, M. S.; et al. Ubiquitous formation of bulk dirac cones and topological surface states from a single orbital manifold in transition-metal dichalcogenides. *Nat. Mater.* **2018**, *17*, 21–28.
- (17) Clark, O. J.; et al. Fermiology and superconductivity of topological surface states in PdTe₂. *Phys. Rev. Lett.* **2018**, *120*, 156401.
- (18) Parkin, S. S. P.; Friend, R. H. 3d transition-metal intercalates of the niobium and tantalum dichalcogenides. I. Magnetic properties. *Philos. Mag. B* **1980**, *41*, 65–93.
- (19) Parkin, S. S. P.; Friend, R. H. 3d transition-metal intercalates of the niobium and tantalum dichalcogenides. II. Transport properties. *Philos. Mag. B* **1980**, *41*, 95–112.
- (20) Miyadai, T.; et al. Magnetic Properties of Cr_{1/3}NbS₂. *J. Phys. Soc. Jpn.* **1983**, *52*, 1394–1401.
- (21) Togawa, Y.; et al. Chiral magnetic soliton lattice on a chiral helimagnet. *Phys. Rev. Lett.* **2012**, *108*, 107202.
- (22) Hall, A. E.; et al. Magnetic structure investigation of the intercalated transition metal dichalcogenide V_{1/3}NbS₂. *Phys. Rev. B* **2021**, *103*, 174431.
- (23) Van den Berg, J. M.; Cossee, P. Structural aspects and magnetic behaviour of NbS₂ and TaS₂ containing extra metal atoms of the first transition series. *Inorg. Chim. Acta* **1968**, *2*, 143–148.
- (24) Xie, L. S.; Husremovic, S.; Gonzalez, O.; Craig, I. M.; Bediako, D. K. Structure and magnetism of iron-and chromium-intercalated niobium and tantalum disulfides. *J. Am. Chem. Soc.* **2022**, *144*, 9525–9542.
- (25) Sirica, N.; et al. The nature of ferromagnetism in the chiral helimagnet Cr_{1/3}NbS₂. *Commun. Phys.* **2020**, *3*, 65.
- (26) Xie, L. S.; et al. Comparative electronic structures of the chiral helimagnets Cr_{1/3}NbS₂ and Cr_{1/3}TaS₂. *Chem. Mater.* **2023**, *35*, 7239–7251.
- (27) Yang, X. P.; et al. Visualizing the out-of-plane electronic dispersions in an intercalated transition metal dichalcogenide. *Phys. Rev. B* **2022**, *105* (12), L121107.
- (28) Popčević, P.; et al. Role of intercalated cobalt in the electronic structure of Co_{1/3}NbS₂. *Phys. Rev. B* **2022**, *105*, 155114.
- (29) Lu, K.; et al. Canted antiferromagnetic order in the monoaxial chiral magnets V_{1/3}TaS₂ and V_{1/3}NbS₂. *Phys. Rev. Mater.* **2020**, *4*, 054416.
- (30) Kousaka, Y.; et al. Chiral helimagnetism in T_{1/3}NbS₂ (T=Cr and Mn). *Nucl. Instrum. Methods Phys. Res. A* **2009**, *600*, 250–253.
- (31) Hall, A. E.; et al. Comparative study of the structural and magnetic properties of Mn_{1/3}NbS₂ and Cr_{1/3}NbS₂. *Phys. Rev. Mater.* **2022**, *6*, 024407.
- (32) Togawa, Y.; et al. Interlayer magnetoresistance due to chiral soliton lattice formation in hexagonal chiral magnet CrNb₃S₆. *Phys. Rev. Lett.* **2013**, *111*, 197204.
- (33) Mayoh, D. A.; et al. Giant topological and planar hall effect in Cr_{1/3}NbS₂. *Phys. Rev. Res.* **2022**, *4*, 013134.
- (34) Wu, X.; et al. Highly tunable magnetic phases in transition-metal dichalcogenide Fe_{1/3+δ}NbS₂. *Phys. Rev. X* **2022**, *12*, 021003.
- (35) Little, A.; et al. Three-state nematicity in the triangular lattice antiferromagnet Fe_{1/3}NbS₂. *Nat. Mater.* **2020**, *19*, 1062–1067.
- (36) Nair, N. L.; et al. Electrical switching in a magnetically intercalated transition metal dichalcogenide. *Nat. Mater.* **2020**, *19*, 153–157.
- (37) Edwards, B.; et al. Giant valley-zeeman coupling in the surface layer of an intercalated transition metal dichalcogenide. *Nat. Mater.* **2023**, *22*, 459–465.
- (38) Sirica, N.; et al. Electronic structure of the chiral helimagnet and 3d-intercalated transition metal dichalcogenide Cr_{1/3}NbS₂. *Phys. Rev. B* **2016**, *94*, 075141.
- (39) Saika, B. K.; et al. Signature of topological band crossing in ferromagnetic Cr_{1/3}NbSe₂ epitaxial thin film. *Phys. Rev. Res.* **2022**, *4*, L042021.
- (40) Tanaka, H.; et al. Large anomalous hall effect induced by weak ferromagnetism in the noncentrosymmetric antiferromagnet CoNb₃S₆. *Phys. Rev. B* **2022**, *105*, L121102.
- (41) Perdew, J. P.; Burke, K.; Ernzerhof, M. Generalized gradient approximation made simple. *Phys. Rev. Lett.* **1996**, *77*, 3865–3868.
- (42) Kresse, G.; Furthmüller, J. Efficient iterative schemes for ab initio total-energy calculations using a plane-wave basis set. *Phys. Rev. B* **1996**, *54*, 11169–11186.
- (43) Kresse, G.; Joubert, D. From ultrasoft pseudopotentials to the projector augmented-wave method. *Phys. Rev. B* **1999**, *59*, 1758–1775.
- (44) Sunko, V.; et al. Maximal Rashba-like spin splitting via kinetic-energy-coupled inversion-symmetry breaking. *Nature* **2017**, *549*, 492–496.
- (45) Siemann, G.-R.; et al. Spin-orbit coupled spin-polarised hole gas at the CrSe₂-terminated surface of AgCrSe₂. *NPJ. Quantum Mater.* **2023**, *8* (1), 61.
- (46) Heil, C.; Schlipf, M.; Giustino, F. Quasiparticle GW band structures and Fermi surfaces of bulk and monolayer NbS₂. *Phys. Rev. B* **2018**, *98*, 075120.
- (47) El Youbi, Z.; et al. Fermiology and electron-phonon coupling in the 2H and 3R polytypes of NbS₂. *Phys. Rev. B* **2021**, *103*, 155105.
- (48) Qin, N.; et al. Persistent exchange splitting in the chiral helimagnet Cr_{1/3}NbS₂. *Phys. Rev. B* **2022**, *106*, 035129.
- (49) Edwards, B.; et al. *Chemical trends of the bulk and surface termination-dependent electronic structure of metal-intercalated transition metal dichalcogenides (dataset)*; University of St Andrews Research Portal, 2024.